

Strength and Cracking Behavior of Frozen Sandstone Containing a Pre-existing Flaw under Impact Load

Boyu Yao^{1,*}, Yuzhe Qiao¹ and Yunfeng Feng¹

¹College of Architecture and Civil Engineering, Xi'an University of Science and Technology, Xi'an 710054, Shaanxi, China.

Received 25 June 2022; Accepted 19 November 2022

Abstract

During engineering construction in natural and artificial frozen rock regions, safety accidents are often caused by the instability and cracking of frozen surrounding rocks resulting from dynamic disturbance. To explore the mechanical properties and crack propagation characteristics of fractured sandstone under impact load at different negative temperatures, impact compression experiments were conducted on fractured sandstone specimens with fissure dip angles of 0°, 15°, 30°, 45°, 60°, 75°, and 90° at temperatures of 0 °C, -2 °C, -4 °C, -6 °C, -8 °C, -10 °C, -15 °C, and -20 °C by applying a split Hopkinson pressure bar with a diameter of ϕ 50 mm. The mechanical properties were analyzed, and the entire process of crack initiation, propagation, coalescence, and destruction was recorded, thus analyzing the influencing mechanism of prefabricated fissure dip angles on cracks from the debonding mode of the ice-rock interface. Results show that the peak stress of sandstone increases with the decreasing temperature, and the existence of fissures reduces the dynamic mechanical properties so that the peak strength decreases and the strain at failure increases. Most of the cracks demonstrate tensile properties, and there accordingly are three failure modes, namely, tensile failure, compression-shear failure, and mixed failure depending on different fissure dip angles. The failure mode of the ice-rock interface determines the cracking behavior and dynamic mechanical properties of frozen fractured rock. The obtained conclusions can provide a theoretical reference for engineering construction safety in cold regions.

Keywords: Frozen fractured sandstone, Dynamic compression, Destruction mode, Impact load

1. Introduction

Natural rock masses feature extensive defects, such as joints, fissures, and structural planes, due to a series of geological processes, such as long-term geotectonic movement, weathering, and denudation. The instability and destruction of rock masses is usually a dynamic evolutionary process in which primary or secondary fissures continuously close, crack, propagate, and coalesce under load [1–2]. In the natural environment, severe low temperatures are common in high-altitude and -latitude areas. In water-rich rock strata, water penetration of fissures can lead to water-ice phase transition at low temperatures, and the generated frost-heave force causes geological and engineering disasters, such as landslide, and damage to tunnel lining. When engineering construction is carried out in such environments, the operation of construction machinery disturbs the rock mass, causing the cracking of frozen rock masses and jeopardizing the life and property safety of the construction personnel.

Many studies have been conducted on frozen fractured rock mass. Wiknerl et al.[3] found that the frost-heave force of porous ice in rocks increases with the decreasing temperature under standard atmospheric pressure. Kosrtomtiinov et al.[4] analyzed the influence of size on the strength of frozen rocks. Park et al.[5] conducted laboratory experiments on South Korean granite and sandstone and found that the thermal conductivity of rocks increases with the decreasing temperature. Freeze-thaw damage is of great importance in the study of frozen fractured rock masses. The frost-heave force caused by the condensation of pore water

in rock into ice is the main cause of freeze-thaw damage. Chen et al.[6] conducted freeze-thaw experiments on welded tuff with varied degrees of water saturation and found that the degree of saturation below 60% has little impact on rock deterioration and that over 70% can cause significant damage to rocks. Ren et al.[7] reported that damage and failure first occurs at the edge of the water-saturated red sandstone specimens in the freeze-thaw cycle experiment, the failure and strength degradation becomes increasingly serious and obvious with the increase of the number of freeze-thaw cycles, and the secondary cracks increase significantly after failure. For the research on moisture and heat migration test, Lin et al.[8] studied the characteristics of the frost-heave force within joints by establishing a 3D model considering the loss of moisture migration during the freeze-thaw process and showed that the moisture migration within joints gradually occurs with the increasing cycle number, and the frost-heave force significantly decreases without water replenishment. In the above-mentioned studies, researchers studied frozen fractured rock masses in terms of their physical and mechanical characteristics, freeze-thaw damage, and moisture migration. However, the indoor test research on frozen fractured rock is relatively limited, and the sampling of rock materials is difficult. Therefore, exploring the crack propagation and destruction mode of frozen fractured rock masses under impact load is important in enriching the test theory and evaluating the damage degree of frozen rock masses.

Impact load refers to the large deformation of materials within a short time. In the study of dynamic rock mechanics, split Hopkinson pressure bar (SHPB) devices are often used

*E-mail address: 850276951@qq.com

ISSN: 1791-2377 © 2022 School of Science, IHU. All rights reserved.

doi:10.25103/jestr.155.16

to simulate dynamic loads on rocks from mechanical impacts, blasting, and explosions. The loading rate has a significant influence on the mechanical properties of a rock mass, such as its compressive and tensile strengths. Different loading rates have different effects on the crack propagation speed, dynamic fracture toughness, and energy release rate. Yao et al. [9] conducted medium- and high-strain rate experiments using a SHPB device and analyzed the dynamic type-II fracture mode of the rocks using X-ray and computed tomography (CT) techniques. Li et al. [10] and Ayatollahi and Aliha [11] performed numerical analysis on the dynamic mixed-mode I/II fractures of semi-circular fractured rocks and concluded that the type-II fracture toughness increases with the loading rate. Natural rock masses may contain fissures with different angles, and their fracture evolution is affected by the fissure dip angles. Xiao et al. [12] conducted impact tests on granite specimens with different fissure dip angles using SHPB and digital image correlation (DIC) methods, finding that the dynamic strength of a 45° specimen is lower than that of a 90° specimen. Li et al. [13] conducted dynamic impact tests on coal-rock assemblages with different fissure dip angles, finding that the fissures in the coal segment has a great influence on the strength of the specimen, with the angle of 30° having the greatest influence. Li et al. [14] conducted dynamic impact tests on fractured rectangular marble specimens and examined the influences of fissure angle on rock's dynamic mechanical properties, fracture behavior, and energy evolution characteristics. Han et al. [15] used a SHPB device to conduct dynamic impact tests on green sandstone specimens with double elliptical fissures. They explored the effects of fissures with different geometric shapes and dip angles on the dynamic strength, deformation performance, and fracture evolution of rock materials. Their experimental results show that the fissure dip angle has a great influence on the dynamic strength, peak strain, and other mechanical properties of different specimens. With the improvements in computational performance, the study of fractured rock masses through numerical simulation has gradually become a useful research method [16–18]. Cracks in fractured rocks propagate at high speed under dynamic loads. To directly analyze the development of cracks, high-speed photography and DIC are widely used in experiments [19–20].

In the past few decades, extensive dynamic studies on fractured sandstone have been carried out at normal temperatures. However, the temperature of a rock mass changes according to the natural environment. In high-altitude and -latitude areas, freezing temperatures cause the water in fractures to freeze and expand, which does not occur in saturated fractured rock masses at normal temperatures. At present, intact specimens are mostly used in dynamic experiments on frozen sandstone. Shan et al. [21] conducted static–dynamic experiments on red sandstone at –15 °C, established a constitutive model composed of destructed, viscoelastic, and elastic bodies, and determined the relationship between the destruction forms of frozen red sandstone and the average strain rate. Bai et al. [22] conducted experiments with a split Hopkinson pressure bar to test the dynamic Brazilian splitting of saturated sandstone at normal temperature and four freezing temperatures. They observed the macroscopic fracture roughness and microscopic fracture morphology of specimens at different temperatures and explained the brittle–ductile transition phenomenon of the microscopic fracture morphology. Few dynamics studies have been carried out on frozen fissures. Yang et al. [23] conducted a dynamic splitting test on frozen

red sandstone. The test showed that the freezing temperature would affect the tensile strength and fracture morphology of sandstone. The above-mentioned studies have made important contributions to the research on the dynamics of frozen fractured rock masses. However, the analysis on low temperature fracture propagation and morphology is still inadequate, thus posing hidden dangers to engineering construction in cold areas.

Previous research on frozen rock masses in terms of dynamics mostly focused on normal-temperature intact and fractured rock masses. However, the mechanical property of rock mass and the initiation of cracks under freezing conditions differ greatly from those at normal temperature. The volume expansion caused by the water–ice phase transition of fractured ice can deteriorate fractured rock masses, and the bonding force between ice and rock enhances the mechanical property of rock masses. The research on frozen rock masses has been mostly carried out under low strain rates and at a single temperature; the disturbance to rock masses in practical engineering is usually mechanical impact load, and the environmental temperature changes with the local climate, latitude, altitude, and engineering environment. Therefore, this experiment carries out a uniaxial test on a sufficient number of prefabricated fractured sandstones with different dip angles under low temperatures and impact load, supporting the research on rock mechanics and crack propagation under the coupling of multiple factors.

In this study, medium-coarse-grained yellow sandstone with seven kinds of prefabricated single fissure with different dip angles (0°, 15°, 30°, 45°, 60°, 75°, and 90°) was impacted and compressed under eight negative temperatures (0 °C, –2 °C, –4 °C, –6 °C, –8 °C, –10 °C, –15 °C, and –20 °C). High-speed photography was adopted to analyze the dynamic characteristics and destruction laws of fractured rocks with different fissure angles at low temperatures and the same fissure angle at different temperatures. The results provide a theoretical basis for engineering projects in cold areas that are affected by dynamic hazards.

2. Materials and methods

2.1 Specimen design and preparation

The experiment used fresh intact rock specimens of medium-coarse-grained yellow sandstone. According to the International Society for Rock Mechanics and Rock Engineering standards, cylindrical specimens with a diameter of 50 mm and a height of 50 mm were processed. An improved high-pressure waterjet cutting equipment was used to prefabricate fissures in the specimens, which were cut in the center with seven different dip angles (0°, 15°, 30°, 45°, 60°, 75°, and 90°) relative to their axis. The length and width of the fissures are 2.0 and 0.1 cm, respectively.

To ensure the reliability and accuracy of the experimental results, individual specimens showing great differences in wave speed were removed. In addition, the flatness of the end surfaces was kept within 0.5 mm and the parallelism within 0.02 mm. Fig. 1 shows a saturated frozen specimen ($\alpha = 45^\circ$). Fissure dip angle α is defined as the angle at which the axis rotates clockwise, d is for the basal diameter of the cylindrical specimen, and h is the height.

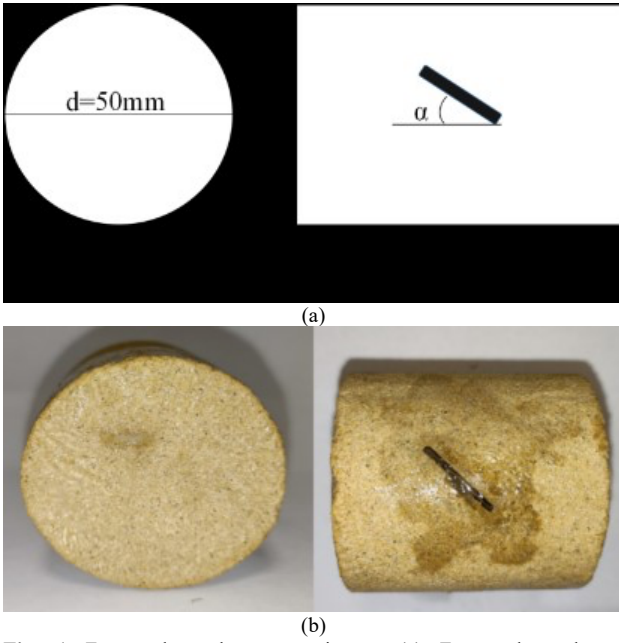


Fig. 1 Fractured sandstone specimens. (a) Fractured sandstone specimens (b) Frozen fractured sandstone specimens

2.2 Test devices and loading scheme

A $\Phi 50\text{mm}$ SHPB was adopted for the dynamic impact experiment with frozen fractured sandstone. The main components of the device are as follows: a power-driven system, a pressure bar system, a data acquisition system, and a computer processing system. During the experiment, a bullet hit the incident bar to generate a propagating stress wave. The strain signal generated on the pressure bar was converted into a voltage signal, amplified by a super dynamic strain gauge, and then displayed by the computer system and an oscilloscope. The SHPB system used in this experiment is illustrated in Fig. 2.

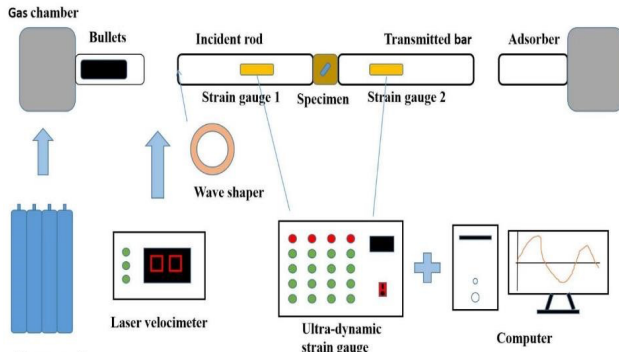


Fig. 2 SHPB experimental system

Before the impact experiment, the specimens were evacuated in a vacuum exhaustor and kept under vacuum for 4 h. Then, the specimens were soaked in distilled water for more than 48 h until their pores were completely saturated. The specimens were wrapped with preservative film to ensure their saturation during the freezing process. Then, the specimens were placed in a low-temperature box for the first freezing at $-2\text{ }^\circ\text{C}$ for 24 h, taken out and injected with water through their fissures, and then frozen for another 24 h at the corresponding experimental temperature. After freezing, the specimens were used in the impact experiments.

The frozen cylindrical specimens were clamped smoothly between the incident and transmitted bars during the impact tests, with the impact pressure set to 0.16 MPa.

The vent valve was activated to push the cylindrical bullet for horizontal axial impact loading (5.5 m/s). The super dynamic strain gauge and a high-speed camera were started simultaneously to observe and record the rock's dynamic response and crack expansion characteristics. The camera framerate was set to 100,000 fps. The tests were repeated 3 or 4 times at each impact rate. The frozen specimens were taken out of the environmental chamber immediately before the impact tests were conducted, and their temperature change during the test was ignored because the tests were conducted with a very short time.

2.3 Experimental principles

The SHPB experiment was based on the assumption of uniform stress and one-dimensional stress wave transmission theory. The "three-wave approach" to data processing and calculation was adopted [24]:

$$\left. \begin{aligned} \sigma(t) &= \frac{E_c A_c}{2A_s} [\varepsilon_I(t) + \varepsilon_R(t) + \varepsilon_T(t)] \\ \varepsilon(t) &= \frac{C_c}{l_s} \int_0^t [\varepsilon_I(t) - \varepsilon_R(t) - \varepsilon_T(t)] dt \\ \dot{\varepsilon}(t) &= \frac{C_c}{l_s} [\varepsilon_I(t) - \varepsilon_R(t) - \varepsilon_T(t)] \end{aligned} \right\} \quad (1)$$

In the formula, $\varepsilon_I(t)$, $\varepsilon_R(t)$, and $\varepsilon_T(t)$ denote the strain signals of the collected incident, reflected, and transmitted waves, respectively; E_c , A_c , and C_c are the elastic modulus, cross-sectional area, and longitudinal wave velocity of the pressure bar, respectively; and A_s and l_s are the cross-sectional area and length of the specimens, respectively.

2.4 Stress equilibrium analysis of dynamic compression test

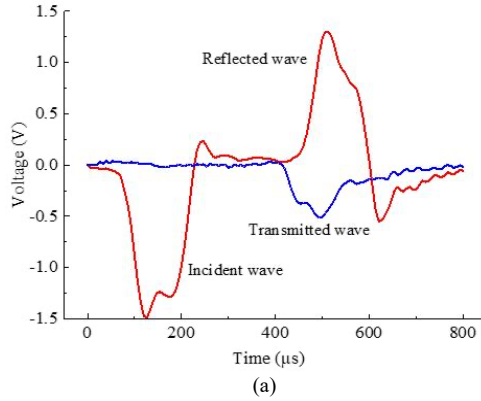
Unlike an intact rock block, a stress wave is affected by fissures during propagation in a fractured rock mass. According to one-dimensional stress wave theory and the assumption of uniform stress, if the stress wave propagates three to four times in the specimen, then uniform stress can be achieved inside the specimen. To ensure the validity of the experimental data, the stress wave collected in the SHPB experiment should be verified first.

According to the basic physical and mechanical parameters of the sandstone specimens, the longitudinal wave velocity was 2670 m/s, and the specimen height was 5 cm. According to the calculations, $75\text{ }\mu\text{s}$ were required for the stress wave to reflect four times in the specimen. Figure 3 shows the voltage time history and stress equilibrium curves of an intact specimen at $-2\text{ }^\circ\text{C}$.

Figure 3 (a) shows that the incident wave's rising time in the specimen exceeded $120\text{ }\mu\text{s}$, indicating that the stress wave was reflected in the specimen at least six times. Therefore, uniform stress was achieved inside the specimen.

Figure 3 (b) indicates that by controlling the initial impact speed, the incident stress of the specimen was approximately 150 MPa, and the crests of the incident stress waves in different specimens were essentially the same, indicating the consistency of the initial conditions during the loading process. A reflected stress wave was generally smaller than an incident wave, but their crest locations basically coincided, and the stress curves of the incident and reflected waves basically overlapped with the transmitted wave. This phenomenon indicates that the specimens

generally met the experimental conditions of stress equilibrium and demonstrated the reliability and robustness



of the experimental data.

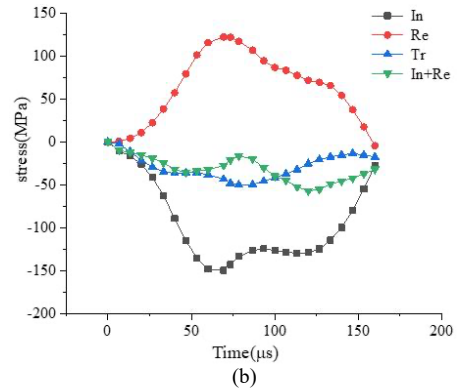


Fig. 3 Voltage–time history curve and stress equilibrium curve of an intact specimen at $-2\text{ }^{\circ}\text{C}$. (a) Voltage–time history curve (b) Stress equilibrium curve

3. Result analysis and discussion

3.1 Stress–strain curves of frozen fractured sandstone

The stress–strain curves of the specimens under impact loading were obtained (Fig. 4) after processing the data using Equation 1.

Generally, the stress–strain curves of the specimens with different fissure dip angles under impact loading are relatively similar in form with four stages: elastic rising, yielding, instability, and residual strength. The change trends are the same and can be divided into three typical stages. Stage I is the linear elastic deformation stage, where the strain increased continuously with the stress. The slope remained the same, so the slope in this stage is defined as the dynamic elastic modulus of the sandstone. Stage II is the plastic stage, where the stress growth rate slowed with the increase in strain rate. With the increasing stress and accumulation of elastic energy in the elastic stage, the elastic energy release began after the yield limit of the specimen

was reached. Then, the internal micro-fissures and -voids in the rock began to initiate, propagate, and coalesce. Stage III is the destruction stage, where the curve gradually decreased with the increase in strain, and the cracks inside the specimen kept expanding to the point of macro destruction and loss of bearing capacity beyond the peak stress, although a certain amount of integrity was maintained.

The analysis of the stress–strain curves of the specimens with different fissure dip angles under impact loading reveals that the linear elastic phases generally overlapped. The peak strains exhibited greater drops than those of the intact specimens, but their peak stresses did not differ much. The peak strength and strain of the specimens changed according to the fissure dip angle and changed more than those of the intact specimens because the prefabricated fissures were first closed, resulting in increased strain when the specimens were destroyed.

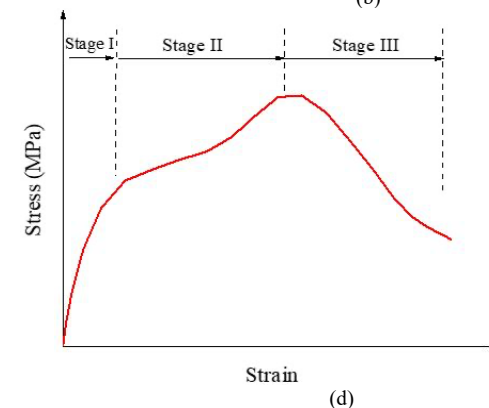
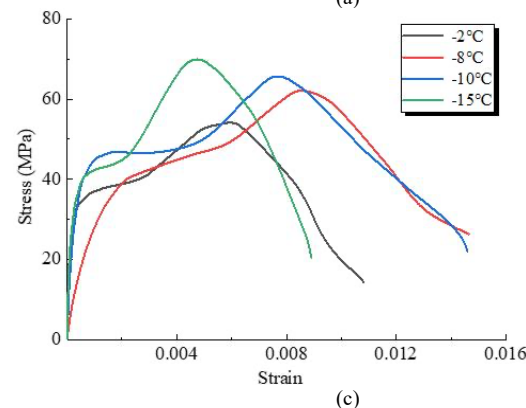
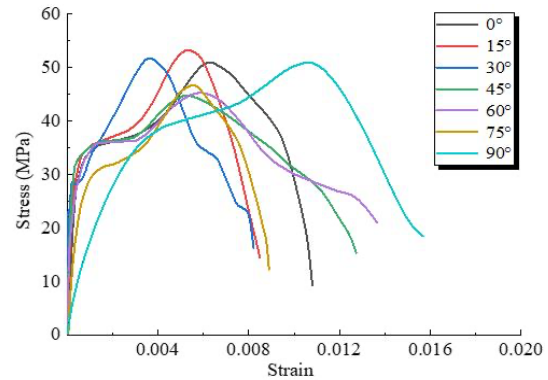
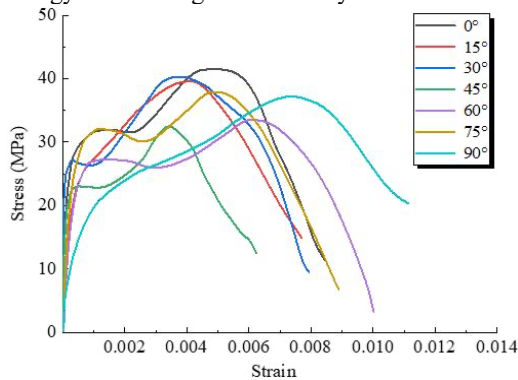


Fig. 4 Stress–strain curves of sandstone subjected to impact tests. (a) $T = -8\text{ }^{\circ}\text{C}$ (b) $T = -15\text{ }^{\circ}\text{C}$ (c) Intact specimens (d) Diagram of phase division

3.2 Changes in peak stress and elastic modulus with fissure dip angle

The peak stress is the ultimate load capacity of a rock material when it reaches the point of destruction and an important parameter reflecting the load-bearing strength of rocks. The comparison of the intact and fractured specimens in Fig. 5(a) at the same temperature shows that the presence of a fracture significantly lowered the peak stress. With increases in the fissure dip angle, the peak stress decreased and then increased in an approximate V-shape, but the

amplitudinal fluctuation was insignificant. Table 1 shows the peak stresses of the specimens at each fissure dip angle at $-10\text{ }^{\circ}\text{C}$. Compared with the intact sandstone specimens (peak stress of 64 MPa), the peak stresses at each angle were reduced by 25.6%, 28.9%, 35.5%, 47.8%, 45.3%, 29.7%, and 26.9%. The minimum peak stress was 33.4 MPa at $\alpha = 45^{\circ}$, and the maximum peak stress was 46.8 MPa at $\alpha = 90^{\circ}$. However, the effect of the fracture angle on peak stress was not obvious, with decreases of 25.6%–47.8%. The difference between the maximum and minimum stresses was only 13.4 MPa.

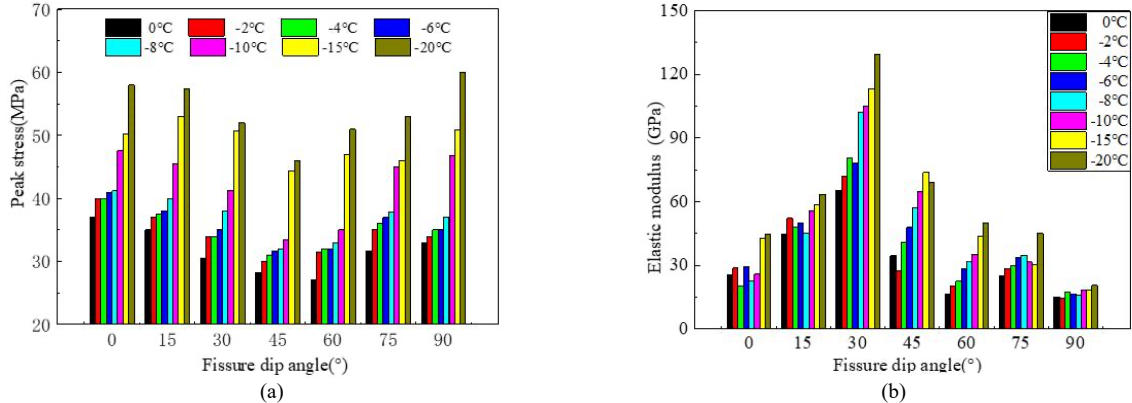


Fig. 5 The influence of fracture dip angle on mechanical properties (a) peak stress. (b) elastic modulus

Table 1. Peak stress at each fissure dip angle at $-10\text{ }^{\circ}\text{C}$

Dip angle ($^{\circ}$)	0	15	30	45	60	75	90
Peak stress (MPa)	64	47.6	45.5	41.3	33.4	35	45
Stress reduction compared with intact specimen	25.6%	28.9%	35.5%	47.8%	45.3%	29.7%	26.9%

The dynamic compressive elastic modulus of rocks is an important parameter characterizing the stiffness of rocks. As shown in Fig. 5(b), the elastic modulus of the specimen increased and then decreased with the increase in fissure dip angle, following an inverted V-shape, with the value increasing and then decreasing for the -15° specimen, reaching a maximum of 113.13 GPa at 30° and a minimum of 18.41 GPa at 90° . Table 2 indicates that, compared with the intact sandstone specimen (elastic modulus = 67.52 GPa), the elastic moduli changed by -36.4% , -12.78% , 67.55% , 9.39% , -35.31% , -55.15% , and -72.7% at the respective

angles, with the greatest increase of 67.55% occurring at $\alpha = 30^{\circ}$, and the smallest elastic modulus occurring at $\alpha = 90^{\circ}$ at which it was 72.73% lower than that of the intact specimens. The elastic modulus was very sensitive to the fissure dip angle. The elastic moduli of the fractured specimens were lower than that of the intact specimen at some dip angles due to the combined effect of the strain rate on the specimen reinforcement and fracture degradation on the specimen. The presence of fissures increased the peak strain at all dip angles.

Table 2. Elastic modulus of specimens with different fissure dip angles at $-15\text{ }^{\circ}\text{C}$

Dip angle ($^{\circ}$)	0	15	30	45	60	75	90
Elastic modulus (GPa)	42.3	58.6	113.1	73.9	43.7	30.1	18.4
Change compared with intact specimens	-36.4%	-12.78%	67.55%	9.39%	-35.31%	-55.15%	-72.7%

3.3 Changes in peak stress and elastic modulus with freezing temperature

As shown in Fig. 6(a), the peak stresses of the specimens with different fissure dip angles exhibited an obvious upward trend with the decrease in temperature. However, the growth rates are uneven; for example, the peak stress increased slowly at $0\text{ }^{\circ}\text{C}$ to $-8\text{ }^{\circ}\text{C}$ and rapidly at $-8\text{ }^{\circ}\text{C}$ to $-15\text{ }^{\circ}\text{C}$. Taking the specimen with $\alpha = 15^{\circ}$ as an example, the peak strengths of the frozen specimens were 35, 37, 37.5, 38, 40, 45.5, 53, and 57.4 MPa. Compared with the specimens at $0\text{ }^{\circ}\text{C}$, the peak strengths were 5.7%, 7.1%, 8.5%, 14.3%, 30%, 51.4%, and 64% higher, respectively. In the range of $0\text{ }^{\circ}\text{C}$ to $-8\text{ }^{\circ}\text{C}$, the average peak strength increased by 1.8% for every $1\text{ }^{\circ}\text{C}$ drop in temperature, while

in the range of $-8\text{ }^{\circ}\text{C}$ to $-15\text{ }^{\circ}\text{C}$, the average increase was 5.3% per $1\text{ }^{\circ}\text{C}$. Similarly, the peak strengths of the specimen with $\alpha = 90^{\circ}$ cracks were 33, 34, 35, 35, 37, 46.8, 50.9, and 60 MPa. At $0\text{ }^{\circ}\text{C}$ to $-8\text{ }^{\circ}\text{C}$, the peak strength increased by 1.5% per $1\text{ }^{\circ}\text{C}$ decrease in temperature, while at $-10\text{ }^{\circ}\text{C}$ to $-15\text{ }^{\circ}\text{C}$, it increased by 6% per $1\text{ }^{\circ}\text{C}$. Table 3 shows the changes in peak stress at $0\text{ }^{\circ}\text{C}$ and $-20\text{ }^{\circ}\text{C}$. The peak stress at different dip angles changed by 56.76%, 64%, 70.49%, 62.77%, 88.89%, 67.3%, and 81.81%, respectively, as the temperature decreased from $0\text{ }^{\circ}\text{C}$ to $-20\text{ }^{\circ}\text{C}$, proving that the decrease in temperature significantly increased the peak stress.

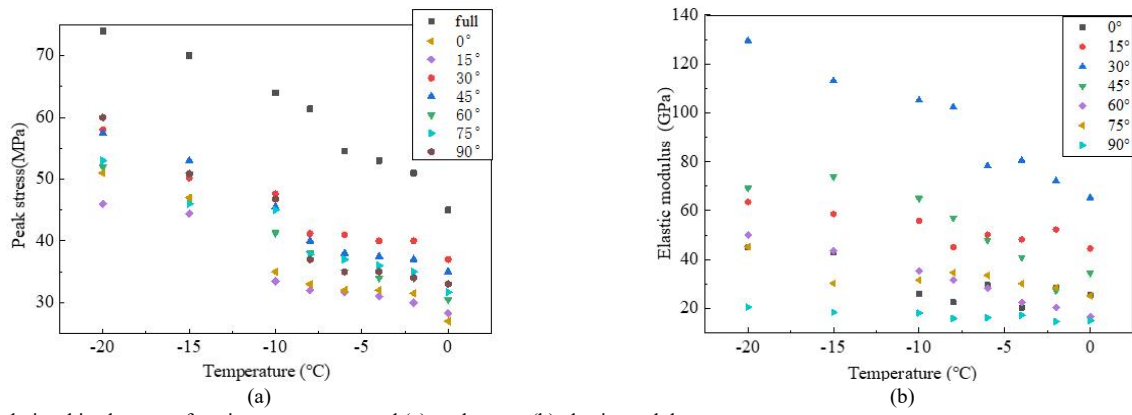


Fig. 6 Relationships between freezing temperature and (a) peak stress (b) elastic modulus

Table 3 Change of peak stress at 0 °C to -20 °C (MPa)

Dip angle (°)	0	15	30	45	60	75	90
0 °C	37	35	30.5	28.3	27	31.7	33
-20 °C	58	57.4	52	46	51	53	60
Increase ratio	57%	64%	71%	63%	89%	67%	82%

As shown in Fig. 6(b), the elastic modulus increased with the decrease in temperature in a similar way as the peak stress, but its sensitivity differed according to the dip angle.

3.4 Crack development law of frozen fractured sandstone

Under impact loads, the specimens exhibited many modes of macro-destruction. Macroscopic cracks were mostly produced by the propagation, convergence, and coalescence of microscopic cracks. Microscopic cracks were produced from microscopic defects, such as micro-fissures and -voids. The randomness of the directions of internal micro-fissures led to the randomness in the directions of microscopic cracks. However, the propagation of macroscopic cracks had no obvious directionality; cracks parallel to the compressive stress direction were tension-type cracks, while those at an angle to the compressive stress direction were shear-type cracks. Tension-type cracks were mainly formed by the propagation of tensile wing cracks and anti-wing cracks, while shear-type cracks were formed by the propagation of coplanar or non-coplanar secondary cracks [25]. The specimens had five types of cracks: wing, anti-wing,

coplanar and non-coplanar secondary, and transverse cracks, as shown in Fig. 7.

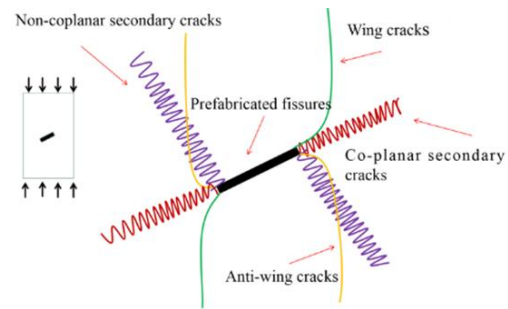
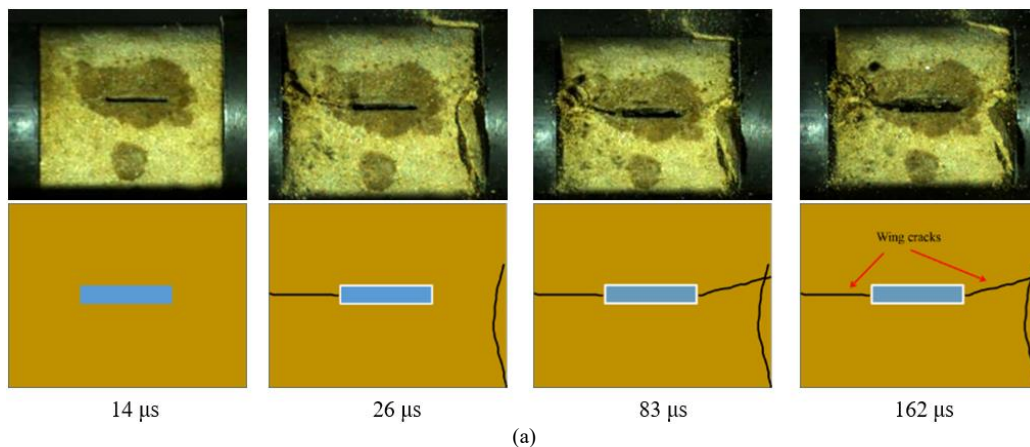
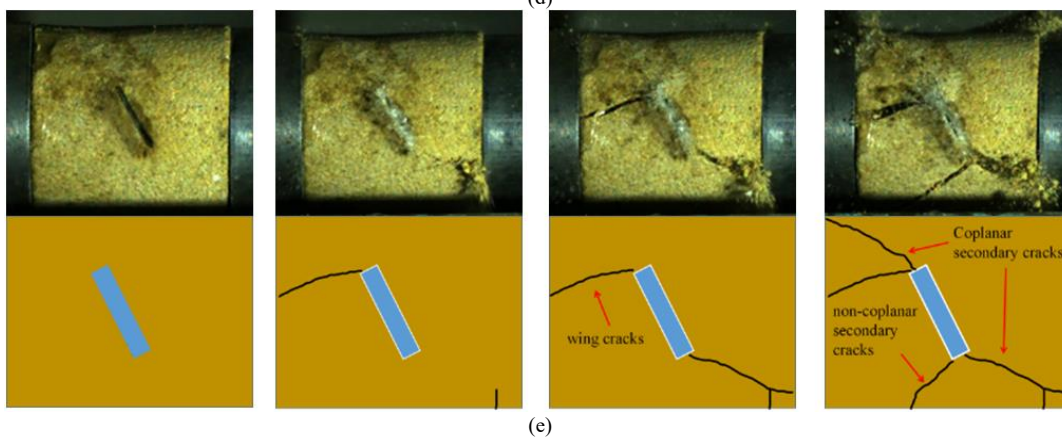
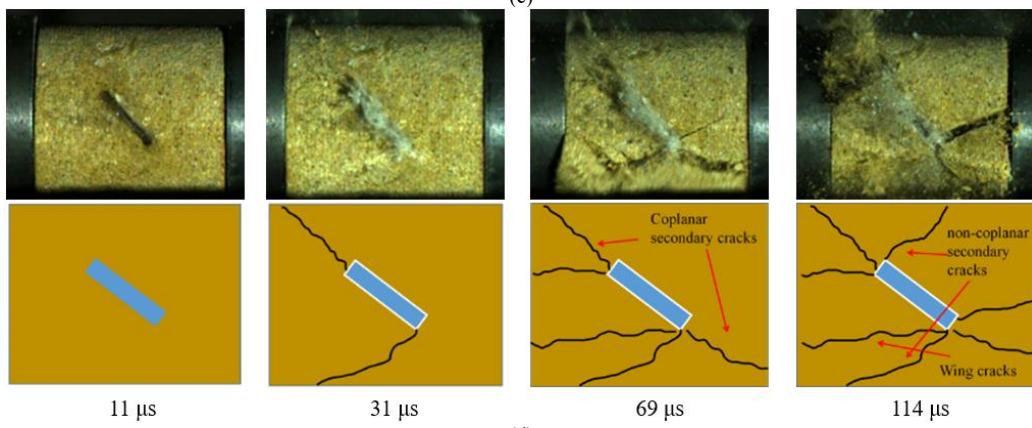
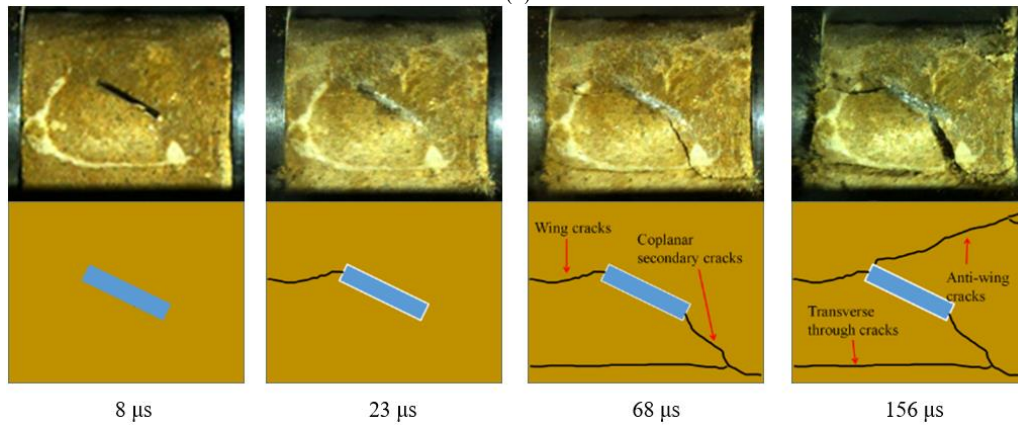
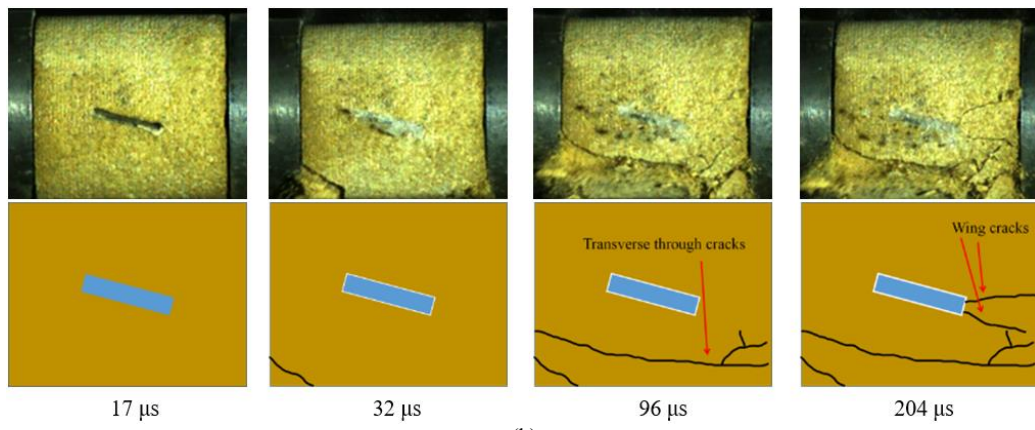


Fig. 7 Type of cracks

A comprehensive analysis of the dynamic compression destruction process at different temperatures shows that the destruction mode and the crack development differed obviously according to the fissure dip angle. However, the changes in destruction mode and crack formation with the decreasing temperature were insignificant. Taking the destruction process of the specimens at -15 °C as an example, Fig. 8 shows the dynamic destruction process of the fractured sandstone captured by high-speed photography.





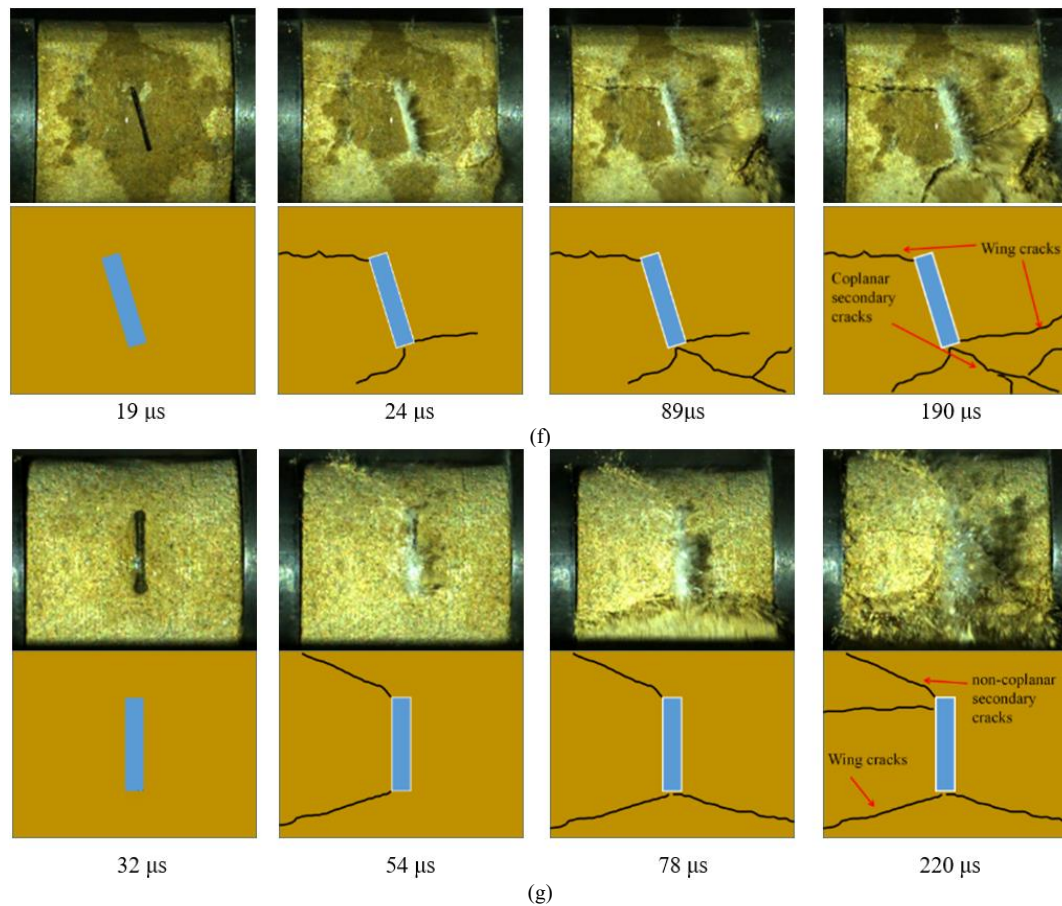


Fig. 8 Dynamic destruction process of fractured sandstone at $-15\text{ }^{\circ}\text{C}$ and different dip angles α Figure. (a) $\alpha = 0^{\circ}$. (b) $\alpha = 15^{\circ}$. (c) $\alpha = 30^{\circ}$. (d) $\alpha = 45^{\circ}$. (e) $\alpha = 60^{\circ}$. (f) $\alpha = 75^{\circ}$. (g) $\alpha = 90^{\circ}$

The analysis of the crack initiation process reveals that when a stress wave passed through a specimen, the fractured ice was destroyed first. Meanwhile, micro-fissures and voids developed and coalesced in the specimen. Then, cracks began to appear at the edges of the prefabricated fissures where stress was concentrated and tended to extend along the prefabricated fissures in the loading direction.

The destruction of most specimens in this experiment was caused by the coalescence of the main crack. Taking Fig. 8(a) as an example, the destruction was caused by a single tension-type crack running through the specimen. Transverse cracks existed widely in specimens with various dip angles. Their formation is related to internal micro-cracks, micro-cavities, and other natural destruction forms, as shown in Fig. 8 (b). Coplanar secondary cracks were the main form of compression shear destruction and often occurred in the specimens with fissure dip angles $> 30^{\circ}$, as shown in Fig. 8(c). As shown in Fig. 8(d,e), in the specimens with $\alpha = 45^{\circ}$ and $\alpha = 60^{\circ}$, the conjugate destruction caused by multiple cracks is easy to occur. Co-occurrence of wing, anti-wing, coplanar secondary, and non-coplanar secondary cracks appeared together in the destruction process. As shown in Fig. 8(f,g), Non-coplanar secondary cracks often appeared in the specimens with an inclination of 60° .

A few of surface cracks appeared in the specimens at high strain rates, and only the main cracks causing final destruction were observable. Some specimens in this experiment, such as those with $\alpha = 0^{\circ}$, 15° , 90° , demonstrated that one or two main cracks could coalesce, resulting in specimen destruction. Some specimens, such as those with $\alpha = 60^{\circ}$, 75° , had branch cracks occurring after the main crack development. The main cracks were mostly wing cracks, such as when $\alpha = 0^{\circ}$, 15° . Coplanar secondary

and wing cracks appeared simultaneously in some specimens, such as those with $\alpha = 45^{\circ}$, 60° . Therefore, under the action of high strain rate, the fissure dip angle had a great impact on the type of crack initiation. The wing cracks at $\alpha = 0^{\circ}$, 15° changed to coplanar secondary cracks at $\alpha = 45^{\circ}$, 60° and then to wing and anti-wing cracks at $\alpha = 75^{\circ}$, 90° . The crack characteristics in this experiment can be summarized as follows. Tension-type cracks appeared in nearly all the specimens in the entire experiment, with wing cracks being their most important macroscopic manifestations. In the experiment, wing cracks were often the first to appear and initiated from the end of the prefabricated fissure and extended to the stress surface with a certain dip angle. Meanwhile, the development of wing cracks was also the main cause of specimen destruction.

Transverse cracks, as a special tensile crack pattern, were formed by the direct connection between the two ends of the stress surface and did not pass through the prefabricated fissures. Coplanar and non-coplanar secondary cracks often appear together with tensile cracks.

3.5 Destruction modes of frozen fractured sandstone

According to the experimental results, the destruction modes of the specimens differ according to their fissure dip angle. The ultimate destruction modes of the rock specimens mainly include compression shear destruction, tensile destruction, and mixed destruction. According to a previous study on crack initiation mechanisms and development tracking [26], cracking can be subdivided into five destruction modes: T-mode (T1, T2), S-mode, and M-mode (M1, M2). As shown in Fig. 9, T-mode destruction is a tensile destruction mode dominated by wing cracks. S-mode destruction is a compression-shear destruction mode, which

is formed by coplanar cracks extending to the edge of the specimen at a certain angle. M-mode destruction involves

the combination of tension and compression-shear cracks.

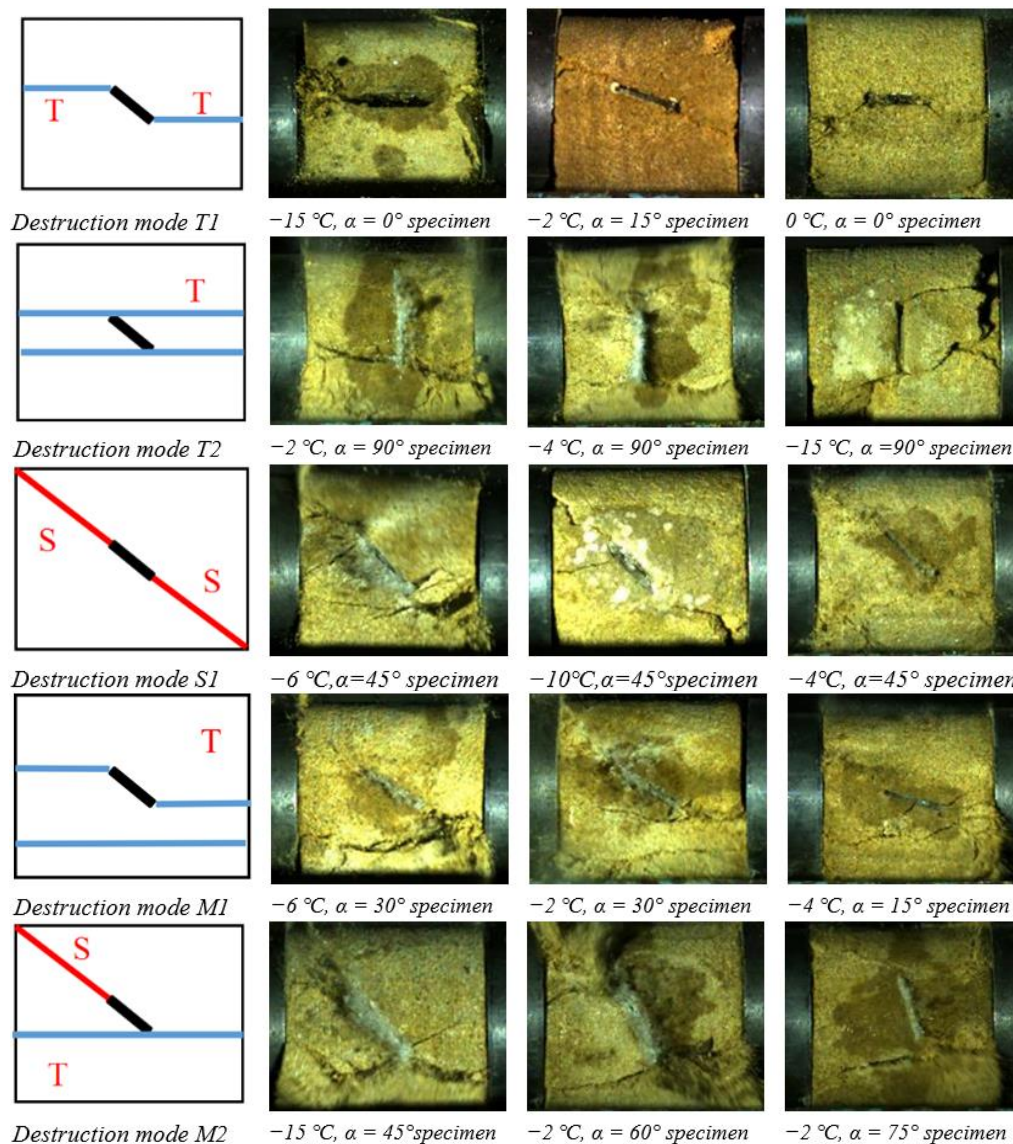


Fig. 9. Diagrams and photographs of fractured sandstone destruction modes

Under impact loading, the strain rates of the specimens were relatively high. Therefore, most of the specimens used in this experiment exhibited tensile or mixed destruction modes, while a few exhibited the compression-shear destruction mode. The tensile destruction mode was mainly caused by wing or anti-wing crack propagation, which often occurred in the specimens with fissure dip angles of $\alpha = 0^\circ, 15^\circ, 90^\circ$. The T1-type tensile destruction was caused by wing cracks due to the stress concentration at the end of the prefabricated fissure, which then extended to the stress surface and often occurred in specimens with $\alpha = 0^\circ, 15^\circ$. In the specimen with $\alpha = 90^\circ$, wing and anti-wing cracks appeared and developed simultaneously until destruction, which was T2-type tensile destruction. When compression-shear destruction occurred, the end of the prefabricated fissure began to crack along the crack direction and extended to the edge of the specimen until destruction occurred. Usually, specimens with $\alpha = 45^\circ$ exhibited S1-type compression shear destruction in many stages. The mixed destruction mode was formed by the combination of shear

and tension destruction. During destruction, wing and anti-wing cracks and coplanar and non-coplanar secondary cracks appeared, usually occurred in one or two crack combinations. The combination of wing and transverse cracks in the M1 mixed destruction mode occurred mostly in the $\alpha = 15^\circ$ specimen. The M2 mixed destruction mode was caused by the combination of coplanar secondary and transverse cracks, which appeared in the compression-shear destruction mode, such as when $\alpha = 45^\circ, 60^\circ, 75^\circ$.

3.6 Influencing mechanism of the destruction mode of frozen fractured sandstone

The destruction modes of frozen fractured sandstone can be classified into tensile destruction, compression-shear destruction, and mixed destruction. This classification is based on the cracking mode, which depends on the separation pattern of the ice-rock interface (Fig. 10).

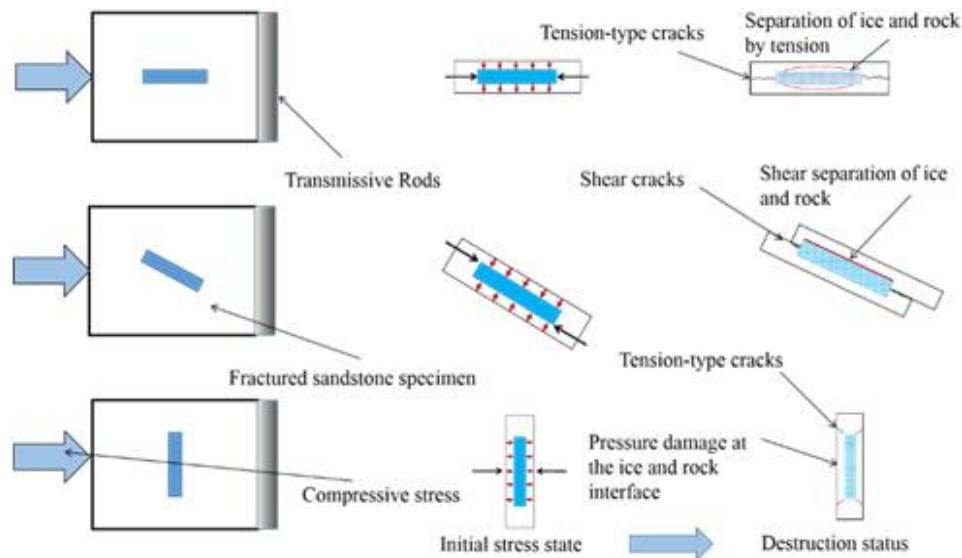


Fig. 10. Diagrams of ice-rock interface destruction

Tension-type destruction is characterized by the stress occurring parallel to the fissure or at a fissure dip angle $\alpha = 0^\circ$. Initially, the fractured ice was pulled but the tensile stress was within the tolerance of the ice's tensile strength. Therefore, cracks did not appear due to the balanced forces. Later, as the tensile stress increased, the fractured ice broke when it could not bear the stress. Then, the ice separated from the rock and no longer bore the tensile stress on the fissure end. Consequently, the increasing stress was concentrated at the fissures. Finally, when the rock at the end of the fissure could not bear the increasing stress, tension-type cracks appeared and extended along the stress direction until the specimen was destroyed, as shown in Fig. 8(a).

When the stress was perpendicular to the fissure ($\alpha = 90^\circ$), the fractured ice was compressed by stress. At first, the compressive stress could not crush the fractured ice. Therefore, the ice-rock interface was not destroyed, and cracks did not appear. When the compressive stress increased to the compressive strength of the ice, the fractured ice broke, and the ice-rock interface failure occurred under compression. After the ice support was lost, the tensile stress gradually concentrated in the middle of the fissure, while the compressive and shear stresses concentrated at the fissure tips. At this time, the cracks were wing and anti-wing cracks, as shown in Fig. 8(g).

When the direction of stress was at a certain angle to the fissure, the compressive stress from the stressed surface was decomposed into shear stress parallel to the fissure and compressive stress perpendicular to the fissure. The compressive strength of the fractured ice and the bonding of the ice-rock interface achieved a balance with the compressive and shear stresses. Two phenomena occurred with the increase in stress. When the ice-rock interface was debonded by shear stress and the fractured ice was not crushed, the shear stress was concentrated at the end of the prefabricated fissure, while the compressive stress was still resisted by the fractured ice. As the shear stress increased and reached the shear strength peak of the fractured end, coplanar secondary cracks of shear properties appeared. The crack extended to the edge of the specimen along the direction of the prefabricated fissure until the specimen was destroyed as a result of shear, which is the compression-shear destruction mode. When the ice-rock interface was destroyed by compressive stress first, the compressive and

shear stresses simultaneously concentrated at the end of the prefabricated fissure after the fractured ice broke. As both compressive and shear stresses could destroy the rock at the end of the fissure, both shear and tensile cracks might have appeared at the end of the fissure. According to the experiment, when the fissure dip angles were $\alpha = 15^\circ, 75^\circ$, tensile cracks mostly appeared in the specimens, and shear cracks mostly appeared in the specimens, when $\alpha = 45^\circ$, as shown in Fig. 8(d).

4. Conclusions

For the crack propagation and engineering disaster in frozen water-rich rock strata, the characteristics of dynamic compression mechanics and the corresponding crack propagation were determined by conducting dynamic compression experiments with frozen sandstone with different dip angles and at different temperatures. The main conclusions are as follows:

(1) Under impact loads, the stress-strain curves of specimens with different fissure dip angles have similar shapes and trends, typically with three stages: linear elasticity, plastic development, and destruction.

(2) Under impact loads, the existence of fissures degraded the mechanical properties of fractured sandstone. The degree of reduction in peak stress was greater in fractured sandstone than in intact specimens at approximately 24.3%–36.6%. However, these values did not change significantly according to the fissure dip angle, generally decreasing first and then increasing before reaching the minimum when $\alpha = 45^\circ$. The elastic modulus was greatly affected by the fissure dip angle, having a V-shaped relationship that peaked at $\alpha = 30^\circ$. Decreases in temperature increased the peak strength and decreased the dynamic elastic modulus of the specimens.

(3) According to the different prefabricated fissure dip angles, the destruction of specimens was of three types: tensile, compression-shear, and mixed. Under impact loads, tensile destruction was common when $\alpha = 0^\circ, 15^\circ, 90^\circ$. Compression-shear destruction occurred frequently when $\alpha = 45^\circ$. In mixed destruction, the specimens were affected by shear and tension, often in specimens with $\alpha = 45^\circ, 60^\circ, 75^\circ$.

(4) The destruction mode of the ice-rock interface could determine the type of cracks first created in the specimens.

When the ice–rock interface was debonded because of tension or destroyed because of compression, tension-type wing cracks first appeared. In contrast, when the ice–rock interface was debonded because of shear before the ice was crushed, shear cracks appeared first.

This study reports the mechanical properties, crack initiation characteristics, and destruction modes of frozen sandstone with different dip angles at different temperatures and proposes the influence of the debonding mode of the ice–rock interface on crack initiation types, contributing to the exploration of fracture propagation in fractured rocks under dynamic disturbance in cold regions and providing guidance in predicting the possible disasters. However, rocks with persistent joints are common in jointed rock masses.

The test specimens in this experiment were all processed as rocks containing non-persistent joints, but great differences may exist in the study of rocks with persistent joints. Therefore, in future studies, rocks with persistent joints should be considered to comprehensively explore the law of fracture propagation and deformation of frozen sandstone under impact load.

This is an Open Access article distributed under the terms of the Creative Commons Attribution License.



References

- Cai M, Kaiser P K, Tasaka Y. "Generalized crack initiation and crack damage stress thresholds of brittle rock masses near underground excavations". *International Journal of Rock Mechanics & Mining Sciences*, 41 (5),2004, pp. 833-847.
- Martin C D, Chandler N A. "The progressive fracture of Lac du Bonnet granite". *International Journal of Rock Mechanics and Mining Sciences & Geomechanics Abstracts*, 31(6),1994, pp. 643-659.
- Winkler E M. "Frost damage to stone and concrete: geological considerations". *Engineering Geology*, 2(5),1968, pp. 315-323.
- Kostromitinov, Nikolenko K N, Nikitin B D . "Testing the strength of frozen rocks on samples of various forms. In Increasing the effectiveness of mining industry in Yakutia. In Russian". *International Journal of Rock Mechanics and Mining Sciences & Geomechanics Abstracts*, 12(2),1975, pp. A20.
- Park C, Synn J H, Shin H S, Cheon DS, LimH D, JeonS W. "An experimental study on the thermal characteristics of rock at low temperatures". *International Journal of Rock Mechanics and Mining Sciences*, 41-supplement 1,2004, pp. 81-86.
- Chen T C, Yeung M R, Mori N. "Effect of water saturation on deterioration of welded tuff due to freeze-thaw action". *Cold Regions Science and Technology*, 38(2/3), 2004, pp. 127-136.
- Ren J X, Yun, M C, Cao X T, Zhang K, Liang Y, Chen X. "Study on the mechanical properties of saturated red sandstone under freeze–thaw conditions". *Environmental earth sciences*, 81(14), 2022, pp. 1-20.
- Lin H, Lei D, Yong R, Jiang C, Du S. "Analytical and numerical analysis for frost heaving stress distribution within rock joints under freezing and thawing cycles". *Environmental earth sciences*, 79(12), 2020, pp. 227-238.
- Yao W, Xu Y, Yu C, Xia K. "A dynamic punch-through shear method for determining dynamic Mode II fracture toughness of rocks". *Engineering Fracture Mechanics*, 3(12), 2017, pp.161-177.
- Li Y, Dai F, Wei M, Du H. "Numerical investigation on dynamic fracture behavior of cracked rocks under mixed mode I/II loading". *Engineering Fracture Mechanics*, 235(6), 2020, pp. 107176.
- Ayatollahi M R, Aliha M R M. "Cracked Brazilian disc specimen subjected to mode II deformation". *Engineering Fracture Mechanics*. 72(4), 2005, pp. 493-503.
- Xiao P, Li D, Zhao G, Zhu Q, Zhang S. "Mechanical properties and failure behavior of rock with different flaw inclinations under coupled static and dynamic loads". *Journal of Central South University*. 2(10), 2020, pp. 2945-2958.
- Li C, Xu Y, Chen P, Li H, Lou P. "Dynamic mechanical properties and fragment fractal characteristics of fractured coal-rock-like combined bodies in split Hopkinson pressure bar tests". *Natural Resources Research*, 29(1), 2020, pp. 3179-3195.
- Li D, Han Z, Sun X, Zhou T, Li X. "Dynamic mechanical properties and fracturing behavior of marble specimens containing single and double flaws in SHPB Tests". *Rock Mechanics and Rock Engineering*, 52(6), 2018, pp. 1623-1643.
- Han Z, Li D, Zhu Q, Liu, M, Sun, Z. "Dynamic fracture evolution and mechanical behavior of sandstone containing noncoplanar elliptical flaws under impact loading". *Advances in Civil Engineering*, 2018(10), 2018, pp. 1-16.
- Yan Z, Dai F, Liu Y, Li A, Du H. "Numerical assessment of the rate-dependent cracking behaviours of single-flawed rocks in split Hopkinson pressure bar tests". *Engineering Fracture Mechanics*, 247(5), 2021, pp. 107656.
- Xu Y, Dai F, Xu N W, Zhao T. "Numerical investigation of dynamic rock fracture toughness determination using a semi-circular bend specimen in Split Hopkinson Pressure Bar Testing". *Rock Mechanics and Rock Engineering*, 49(3), 2016, pp. 731-745.
- Keilegavlen E, Berge R, Fumagalli A, Starnoni M, Stefansson I, Varela J, Berre I. "PorePy: an open-source software for simulation of multiphysics processes in fractured porous media". *Computational Geosciences*, 25(1), 2020, pp. 243-265.
- Dong P, Wu B, Xia K, Wang Q. "Fracture modes of single-flawed rock-like material plates subjected to dynamic compression". *International Journal of Geomechanics*, 20(9), 2020, pp. 1-13.
- Liu X, Dai F, Liu Y, Pei P, Yan Z. "Experimental investigation of the dynamic tensile properties of naturally saturated rocks using the coupled static–dynamic flattened Brazilian disc method". *Energies*, 14(16), 2021, pp. 1-18.
- Shan R, Song Y, Song L, Bai Y. "Dynamic property tests of frozen red sandstone using a split Hopkinson pressure bar". *Earthquake Engineering and Engineering Vibration*, 18(3) 2019, pp. 511-519.
- Bai Y, Shan R, Tong X, Han T, Dou H. "Study on the effect of dynamic disturbance on creep behavior of frozen fractured red sandstone". *Mechanics of Time-Dependent Materials*, 26(1), 2022, pp. 1-21.
- Yang, R., Fang, S., Guo, D. "Study on dynamic tensile strength of red sandstone under impact loading and negative temperature." *Geotechnical and Geological Engineering*, 37(5), 2019, pp.4527–4537.
- Wang T T, Shang B. "Three-wave mutual-checking method for data processing of SHPB experiments of concrete". *Journal of Mechanics*, 30(5), 2014, pp. 5-10.
- Bobet A. "The initiation of secondary cracks in compression". *Engineering Fracture Mechanics*, 66(2), 2000, pp. 187-219.
- Liu Q S, Xu J, Liu X W, Jiang J, Liu B. "The role of flaws on crack growth in rock-like material assessed by AE technique". *International Journal of Fracture*, 193(2), 2015, pp. 99-115.